

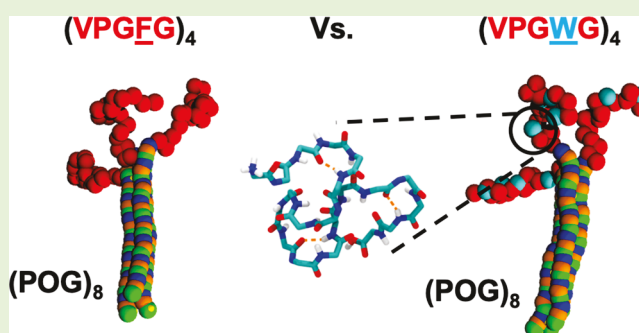
# Effect of Peptide Sequence on the LCST-Like Transition of Elastin-Like Peptides and Elastin-Like Peptide–Collagen-Like Peptide Conjugates: Simulations and Experiments

Ammu Prhashanna,<sup>†,‡</sup> Phillip A. Taylor,<sup>†,‡</sup> Jingya Qin,<sup>†,§</sup> Kristi L. Kiick,<sup>\*,§</sup> and Arthi Jayaraman<sup>\*,‡,§</sup>

<sup>†</sup>Department of Chemical and Biomolecular Engineering, Colburn Laboratory, and <sup>§</sup>Department of Materials Science and Engineering, University of Delaware, 150 Academy Street, Newark, Delaware 19716, United States

## Supporting Information

**ABSTRACT:** Elastin-like polypeptides (ELPs) are thermoresponsive biopolymers that undergo an LCST-like phase transition in aqueous solutions. The temperature of this LCST-like transition,  $T_t$ , can be tuned by varying the number of repeat units in the ELP, sequence and composition of the repeat units, the solution conditions, and via conjugation to other biomacromolecules. In this study, we show how and why the choice of guest (X) residue in the VPGXG pentad repeat tunes the  $T_t$  of short ELPs, (VPGXG)<sub>4</sub>, in the free state and when conjugated to collagen-like peptides (CLPs). In experiments, the (VPGWG)<sub>4</sub> chain (in short, WWWW) has a  $T_t < 278$  K, while (VPGFG)<sub>4</sub> or FFFF has a  $T_t > 353$  K in both free ELP and ELP–CLP systems. The  $T_t$  for the FWWW ELP sequence decreases from being  $>353$  K for free ELP to  $<278$  K for the corresponding ELP–CLP system. The decrease in  $T_t$  upon conjugation to CLP has been shown to be due to the crowding of ELP chains that decreases the entropic loss upon ELP aggregation. Even though the net hydrophobicity of ELP has been reasoned to drive the  $T_t$ , the origins of lower  $T_t$  of WWWW compared to FFFF are unclear, as there is disagreement in hydrophobicity scales in how phenylalanine (F) compares to tryptophan (W). Motivated by these experimental observations, we use a combination of atomistic and coarse-grained (CG) molecular dynamics simulations. Atomistic simulations of free and tethered ELPs show that WWWW are more prone to acquire  $\beta$ -turn structures than FFFF at lower temperatures. Also, the atomistically informed CG simulations show that the increased local stiffness in W than F due to the bulkier side chain in W compared to F, alone does not cause the shift in the transition of WWWW versus FFFF. The experimentally observed lower  $T_t$  of WWWW than FFFF is achieved in CG simulations only when the CG model incorporates both the atomistically informed local stiffness and stronger effective attractions localized at the W position versus the F position. The effective interactions localized at the guest residue in the CG model is guided by our atomistically observed increased propensity for  $\beta$ -turn structure in WWWW versus FFFF and by past experimental work of Urry et al. quantifying hydrophobic differences through enthalpy of association for W versus F.



## 1. INTRODUCTION

Elastin-like polypeptides (ELPs) are a class of synthetic polypeptides comprised of multiple repeats of the amino acid sequence (V-P-G-X-G)<sub>n</sub>, where V, P, and G are valine, proline, and glycine, respectively, and  $n$  is the number of pentamer repeat units along the polypeptide chain. The fourth residue, X, in this pentad is often termed the “guest residue” which can be any amino acid except proline.<sup>1</sup> The V-P-G-X-G repeat unit is derived from the hydrophobic domain of tropoelastin, a precursor of elastin which is an extracellular matrix (ECM) protein that provides elasticity to organs and tissues.<sup>2,3</sup> ELPs undergo a lower critical solution temperature (LCST)-like phase transition in aqueous solutions, which means ELPs are soluble below the transition temperature,  $T_t$ , and insoluble above  $T_t$ .<sup>4–6</sup> Past studies have shown that the  $T_t$  of ELP can be tuned by varying molecular weight, ELP concentration, salt concentration, guest residues, pressure, pH, or by altering the

sequence directionality.<sup>7–16</sup> Due to this thermoresponsive nature and biocompatibility, ELPs are widely used in a variety of applications including drug delivery,<sup>17,18</sup> molecular switches,<sup>19,20</sup> and tissue engineering scaffolds,<sup>21–23</sup> among others.

The origin of LCST-like phase behavior of ELPs has been the subject of numerous experimental and computational studies. In general, the LCST-like phase behavior of ELPs has been mainly attributed to dehydration and hydrophobic effects with increasing temperature,<sup>7,24–29</sup> and formation of secondary structures, specifically  $\beta$ -turns.<sup>5,30–32</sup> Studies also suggest that the number of ELP pentapeptide repeat units impacts the above driving forces with the  $T_t$  decreasing with an increasing

Received: October 13, 2018

Revised: December 14, 2018

Published: February 4, 2019

number of ELP pentapeptide repeat units.<sup>7–9,30</sup> Thus, it is expected that short ELPs either have high  $T_t$  or do not undergo an LCST-like phase transition in the temperature range where water is in a liquid state. As the focus of this paper is the elucidation of the molecular interactions that govern the  $T_t$  for varying ELP sequence in short ELPs, we review the most relevant past studies focused on short ELPs. Several studies have shown that ELPs adopt random coil conformations at temperatures below the  $T_t$  and ordered, secondary structures above the  $T_t$ . For example, Nuhn and Klok<sup>30</sup> found that with increasing temperature there is a decrease in random coil conformations and an increase in the number of configurations with  $\beta$ -turn structure for the ELP sequences with the GVGVP motif. Similarly, in all-atom molecular dynamics simulations Tang et al.<sup>33</sup> observed a higher propensity of (VPGXG)<sub>5</sub> to form  $\beta$ -rich secondary structures in a physiological temperature range (310–315 K) and found that those structural changes of ELP are correlated with water dynamics near ELP and contacts between aliphatic side chains. In another example, Ahmed et al.<sup>31</sup> observed secondary structures in cyclic (VPGVG)<sub>3</sub> and linear GVG(VPGVG)<sub>2</sub> ELP sequences that underwent LCST-like transition. Other studies have suggested entropic driving forces and the related hydrophobic effects as the underlying molecular mechanism of the LCST-like transition. For example, Reichheld et al.<sup>34</sup> studied coacervation of short ELPs with three repeat units and found that a frustrated hydrophobic collapse is promoted by the increased entropic penalty of solvating ELP chains under conditions of high salt and temperature. Krukau et al.<sup>35</sup> who studied GVG(VPGVG)<sub>3</sub> using all-atom MD simulations at zero-salt concentration found breaking of the network of hydration waters enveloping the peptide around the  $T_t$  and the transition from a rigid conformation of ELPs at lower temperatures to a flexible conformation at higher temperatures. They asserted that the conformational transition of hydrated ELPs upon heating is due to the redistribution of populations of various locally ordered structures rather than the folding of ELPs upon heating. In contrast, Rousseau et al.<sup>36</sup> who performed all-atom molecular dynamics (MD) simulations of GVG(VPGVG) at a zero-salt concentration found that, while the extended structural conformations predominate at all temperatures, some compact structures are observed at high temperatures above  $T_t$ . These results agree with Huang et al.<sup>37</sup> who observed an increase in peptide–peptide hydrogen bonds and a decrease in peptide–water hydrogen bonds with increasing temperature for (LGGVG)<sub>3</sub> by performing 20 ns all-atom molecular simulations at a zero-salt concentration. Clearly, these past studies show that there is some debate on the underlying molecular driving forces that govern the  $T_t$  of short ELPs.

Besides the above studies describing the molecular interactions that induce an LCST-like phase transition in short ELPs, there are other studies that have shown that the  $T_t$  of short ELPs can be shifted through addition of salt<sup>25</sup> and conjugation to other macromolecules.<sup>33,38–43</sup> For example, in related work by Luo and Kiick, short ELPs (i.e., 4–6 pentads) conjugated to collagen-like peptides (CLP) exhibit a decrease in  $T_t$  (of >80 °C) when the CLP strands are in a triple helix conformation.<sup>38</sup> Condon, Martin, and Jayaraman have shown that this decrease in  $T_t$  of the ELP–CLP conjugates compared to free ELP is due to the local crowding of ELPs when conjugated to CLP, which impacts the entropic driving forces of the transition.<sup>10</sup> Besides decreasing the  $T_t$  of the short ELPs,

the structure and thermodynamics of CLP triple helices allows the formation of self-assembled nanostructures above the  $T_t$  of ELP–CLP and below the melting temperature of the CLP triple helix ( $T_m$ ).<sup>38</sup> The CLP triple helix is stable at temperatures below its  $T_m$  due to interchain hydrogen bonds formed by three polypeptide chains, each of which is composed of (G-X-Y)<sub>m</sub> repeats, where X and Y are generally proline and hydroxyproline, respectively, and  $m$  is the number of repeat units along the polypeptide.<sup>44</sup> As the temperature is increased these interchain CLP hydrogen bonds melt and the CLP triple helix dissociates into individual strands. The  $T_m$  of the CLP triple helix is a function of the number of G-X-Y repeat units (or  $m$ ) in each CLP strand,<sup>45</sup> the identity of the amino acids located at X and Y positions,<sup>46,47</sup> and solvent quality.<sup>48</sup> Interestingly, Luo and Kiick introduced the idea that one could use the dual-phase transitions of the ELP–CLP diblock conjugates, and the explicit design of ELP and CLP blocks that tailors the  $T_t$  and  $T_m$ , to stabilize self-assembled nanostructures at temperatures in between  $T_t$  and  $T_m$ .<sup>35</sup> Below the  $T_t$  of the ELP–CLP conjugates, the ELP–CLP molecules are soluble in solution, while above the  $T_m$ , the CLP triple helix melts and the single-strand ELP–CLP chains become soluble again, as the  $T_t$  of the single-strand ELP–CLP is shown to be higher than that of the free ELP.<sup>10,38,49</sup> This phase behavior is qualitatively shown in a schematic in [Supporting Information](#) (see [Figure S1](#)). The formation of nanostructures that are stable in a narrow range of temperatures between  $T_t$  and  $T_m$  creates opportunities for designing biocompatible ELP–CLP-based nanomaterials to be utilized under biologically relevant conditions. We tackle one part of this quest in this paper by specifically studying how the ELP pentad composition for short ELPs tunes the  $T_t$  of ELPs and ELPs conjugated to the CLP triple helix.

In this paper, we aim to tune the  $T_t$  of short ELPs conjugated to CLPs by varying the guest residues (i.e., X in VPGXG pentad) to be either F (phenylalanine) or W (tryptophan). Large molecular weight ELPs (approximately 100–120 repeat units), with tryptophan as the guest residue, have been shown to exhibit a lower  $T_t$  than ELPs with phenylalanine as the guest residue.<sup>12</sup> Even though the net hydrophobicity of an ELP pentad has been reasoned to drive the  $T_t$ , the origins of the lower  $T_t$  of WWWW than FFFF are unclear as there are discrepancies in hydrophobicity scales in how phenylalanine (F) compares to tryptophan (W).<sup>50–54</sup> For short ELPs, in free state and upon conjugation to CLPs, we hypothesize that the tryptophan-based ELPs will have a lower  $T_t$  than phenylalanine-based ELPs because: (1) The bulkier aromatic group in the side chains of tryptophan could increase stiffness in ELP chains leading to lower conformational entropy loss upon aggregation<sup>55</sup> and, thus, a lower  $T_t$  compared to phenylalanine-containing ELP chains. (2) As tryptophan is known to form  $\beta$ -hairpins in polypeptides,<sup>56,57</sup> it is possible that in tryptophan-based ELPs, the  $\beta$ -turn structure is dominant, which in turn could stabilize collapsed configurations at lower temperatures, causing a lower  $T_t$  compared to phenylalanine containing ELPs. We use atomistic and coarse-grained (CG) MD simulations along with some experiments to test the above hypothesis (primarily computationally) and provide a molecular-level reasoning for our observations. The atomistic simulations provide the chain conformations and structural transitions such as  $\beta$ -turns in ELPs as a function of temperature. Though the atomistic simulations are able to provide atomically detailed structural

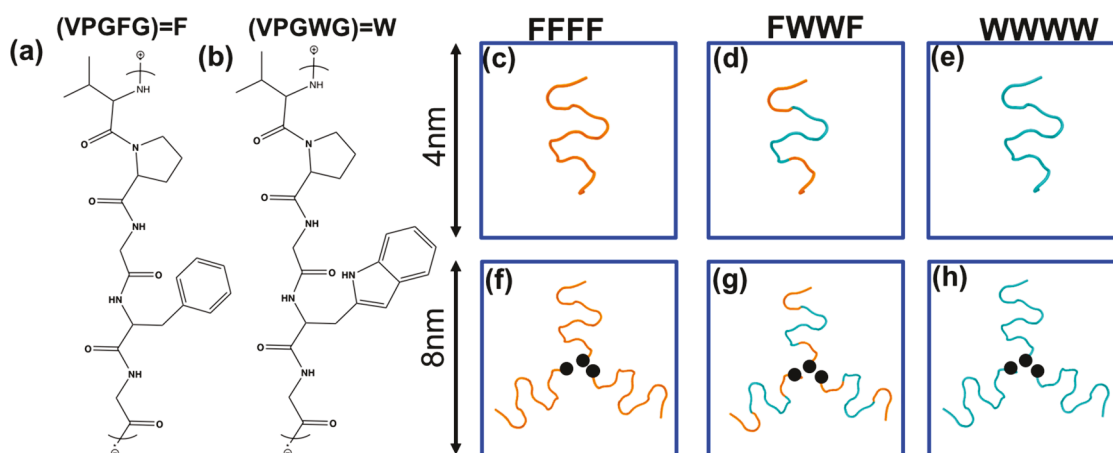


**Figure 1.** Chemical structure of (a) (VPGFG) termed as “F” in short and (b) (VPGWG) termed as “W” in short. Schematics of the initial configuration in atomistic simulations of one free ELP chain (c–e) and three tethered ELP chains (f–h) with FFFF (i.e., (VPGFG)<sub>4</sub>), FWFW, and WWWW sequences, where orange depicts pentads with F in the 4th position and cyan depicts pentads with W in the 4th position. Cubic simulation box sizes of size 4 and 8 nm are used for the free ELP simulations and three tethered ELPs simulations.

analysis of ELP and the surrounding water molecules, it is not feasible to simulate experimentally relevant length scales and ELP–CLP conjugate systems with atomistic detail. Thus, we use atomistically informed CG MD simulations to understand the effect of guest residues on the LCST-like transitions of free ELPs and ELP–CLP conjugates and test the hypothesis stated above.

The paper is organized as follows. In section 2, we describe the details of experimental synthesis and characterization techniques followed by simulation methods (atomistic and CG), systems simulated and computational analysis. In section 3, we present first the results from our experiments which motivate the detailed atomistic and CG simulation work presented next. Finally, we summarize our results in the Conclusions section.

## 2. METHODS

**A. Experimental Protocol.** Chemicals required for peptide synthesis, such as Fmoc-protected amino acids, Rink amide polystyrene resin, *N,N*-diisopropylethylamine (DIEA), and piperidine are purchased from AAPPTec Inc. (Louisville, KY). HPLC-grade acetonitrile and dimethylformamide (DMF) are purchased from Fisher Scientific (Fairlawn, NJ). *N,N,N',N'*-Tetramethyl-*O*-(1*H*-benzotriazol-1-yl)uronium hexafluorophosphate (HBTU), *N*-methyl-2-pyrrolidone (NMP), trifluoroacetic acid (TFA), triisopropylsilane (TIS), triethylamine (TEA), and diisopropylethylamine (DIEA) are purchased from Sigma-Aldrich (St. Louis, MO).

Elastin-like peptides (ELPs) and collagen-like peptides (CLPs) are synthesized via traditional solid-phase peptide synthesis methods (SPPS)<sup>58</sup> using a Focus XC automatic peptide synthesizer (AAPPTec Inc., Louisville, KY). ELPs with sequences (VPGFG)<sub>4</sub>G', (VPGFG)-(VPGWG)-(VPGWG)-(VPGFG)G', and (VPGWG)<sub>4</sub>G' (where G': propargyl glycine), which will be termed here after as FFFF, FWFW, and WWWW, are produced, as are CLPs with the sequence (GPO)<sub>8</sub>GG. The molecular weights of all peptides are verified via ESI-MS: FFFF = 1943 Da, FWFW = 2021 Da, WWWW = 2099 Da, and (GPO)<sub>8</sub>GG = 2380 Da. The N-terminal end of the CLP is then modified on resin to attach an azide, and after cleavage from the resin, the C-terminal end of CLP is amidated. As for the ELP, the N-terminal end of the ELP is left unmodified and the C-terminal end of the ELP is amidated. Next, the synthesis of the ELP–CLP conjugate is performed via the copper(I)-catalyzed azide–alkyne cycloaddition (CuAAC) “click” reaction using synthetic protocols previously reported.<sup>38</sup> An azide group from 4-azidobutanoic acid is introduced to the N terminus of the CLP and an alkyne group from propargyl

glycine is included at the C terminus of the ELP to allow facile conjugation of the two peptides. We do not expect that the triazole linkage should have any significant impact on the assembly properties of these molecules, as the assembly relies on the “bulk” properties of the CLP domain and ELP domain separately. Furthermore, NMR and FTIR are used to confirm that there are no chemical changes in the peptide domains as a result of the click reaction. The obtained peptides are then purified to >95% purity using reverse-phase HPLC and <sup>1</sup>H NMR spectroscopy and FTIR measurements are conducted to confirm the 1:1 stoichiometry of the ELP/CLP conjugate.

The LCST-like phase behavior of the polypeptides is examined by the formation of aggregates/nanoparticles which is observed using dynamic light scattering on a Zetasizer Nano series (Nano ZS, Malvern Instruments, U.K.) at a scattering angle of 173° and data fitting using the cumulant method. All samples are dissolved in deionized water (DI water) at a concentration of 1 mg/mL. For studies of ELP–CLP conjugates, solutions are incubated at 353 K for 10 min and cooled down to room temperature before measurement. The transition temperature of a given ELP–CLP conjugate is obtained by measurement of the average size of nanoparticles at temperatures from 278 to 353 K with an interval of 5 K. Samples are incubated at each temperature for 10 min before measurement. The reported data represent an average of the measurements of at least three different samples.

**B. Atomistic Simulation.** We conduct all-atom molecular dynamics (MD) simulations using the GROMACS 4.6.7<sup>59</sup> package to understand the LCST-like phase behavior of free (VPGXG) based ELPs and tethered ELPs (to mimic conjugation of ELP to CLP). We study three ELP sequences all with four VPGXG pentads with either F and W in the X position (Figure 1a,b), denoted as FFFF, FWFW, and WWWW.

Free ELPs are simulated by placing a single ELP chain in a simulation box mimicking infinitely dilute solution conditions (Figure 1c–e). An atomistically detailed single ELP chain with the appropriate sequence adopting a β-spiral initial configuration is generated using the PyMOL peptide builder tool.<sup>60</sup> We choose the N-terminal end to be charged as VAL-NH<sup>3+</sup> and the C-terminal end to be uncharged as GLY-COOH. To avoid the unfeasible/large computational intensity involving simulation of the ELP conjugated to a CLP triple helix, the impact of CLP conjugation on ELP chains is mimicked in atomistic simulations by arranging three tethered ELPs with the tethering points arranged in a triangle mimicking the CLP triple helix top surface (Figure 1f–h). We choose the distance between the tethered C-terminal ends of the 3 ELPs as ~1.03 nm such that the diameter of a circle encompassing the tethering points triangle is ~1.2 nm, approximately equal to the observed diameter of a CLP triple helix.<sup>38</sup> The tethering of the C-terminal group is done by

imposing a positional restraint on the carbon atom of the C-terminal carbonyl group as described in Condon et al.<sup>10</sup> In GROMACS,<sup>59</sup> positional restraints are harmonic bonds between positions of the peptide atoms at a specific time and the initial positions of those atoms. The harmonic positional restraint is mathematically written as

$$U_{\text{posres}}(x, y, z) = \frac{1}{2}k_{\text{posres}}[(x - x_0)^2 + (y - y_0)^2 + (z - z_0)^2] \quad (1)$$

where  $U_{\text{posres}}$  is the positional restraint potential,  $k_{\text{posres}} = 10^4$  KJ (mol nm<sup>2</sup>)<sup>-1</sup> is the harmonic bond force constant,  $(x, y, z)$  is the position of the atom at a specific time in Cartesian coordinates, and  $(x_0, y_0, z_0)$  is the desired position of the atom, where it is placed initially. We note that, in our simulations, we do not capture the exact chemistries of the end groups as in the experimental studies of free ELP and ELP-CLP. This is to keep the simulation results useful irrespective of the peptide(s) synthesis technique. Since our focus is on the free and tethered ELP chain conformations and secondary structures, we confirm that the C-terminal-OH group does not form explicit hydrogen bonds with the atoms in the ELP chain and, thus, does not impact the ELP chain conformations and structure (see Figure S2).

We use the OPLS-AA/L<sup>61</sup> force field for peptide and TIP4P<sup>62</sup> water model in our simulations. The initial configuration of the ELPs is solvated with TIP4P water molecules in cubic box sizes of 4 and 8 nm for 1 free ELP chain and 3 tethered ELP chains, respectively. As the N-terminus contains a charged group, NH<sub>3</sub><sup>+</sup>, we add an equal number of chloride counterions (Cl<sup>-</sup>) to make the entire simulation box electrostatically neutral. Thus, we add one Cl<sup>-</sup> ion and three Cl<sup>-</sup> ions for a one free ELP chain and three tethered ELP chains systems, respectively. The entire system is first subject to energy minimization using a steepest descent method with the maximum force tolerance level set as 900 KJ·mol<sup>-1</sup>·nm<sup>-1</sup>. Then the molecular dynamics simulation is conducted in the NPT ensemble at desired temperature and 1 bar pressure for 400 and 200 ns for one free ELP chain and three tethered ELP chains, respectively. We simulate at temperatures ranging from 278 to 370 K to mimic the experimental temperature range. For these MD simulations, we use a time step of 2 fs as the bonds that move with a higher frequency are constrained via the LINCS<sup>63</sup> method. Temperature coupling is achieved via a stochastic velocity rescaling method,<sup>64</sup> while, for pressure coupling, we use the Berendsen barostat.<sup>65</sup> The time constants for the temperature and pressure couplings are 0.1 and 2.0 ps, respectively. Electrostatic interactions are modeled using particle-mesh Ewald (PME) method<sup>66</sup> using fourth order cubic interpolation.

From the configurations obtained from the atomistic MD simulations, we quantify the persistence length of the polymer defined as<sup>67</sup>

$$L_p = \frac{\langle \vec{R}_{ee} \cdot \vec{b}_1 \rangle}{\langle b \rangle} \quad (2)$$

where  $\vec{R}_{ee}$  and  $\vec{b}_1$  are the end-to-end distance vector and first bond vector, respectively.  $b$  is the bond length and  $\langle \dots \rangle$  represents an ensemble average. The bond vectors of the ELP chains are always numbered from the N-terminal group and thus, the first bond vector corresponds to the atoms near the N-terminus. The persistence length of free ELP chains is calculated using the data from 200 to 400 ns part of the trajectory and dividing that last 200 ns data into three blocks. We report the mean and standard deviation of the three block averages. In the 200–400 ns of the simulation trajectory for one free ELP system and 100–200 ns of the simulation trajectory for three tethered ELPs systems, the potential energy of the system is fairly constant with reasonable fluctuations. This along with our past experience simulating slightly longer ELP chains in Condon et al.<sup>10</sup> suggests that this is sufficient time for equilibration (see, for example, this information for WWW at 278 K shown in Figure S3).

To quantify the local stiffness around the guest residue, we calculate the bond angle distributions of G<sub>X</sub>G in each VPG<sub>X</sub>G. The probability density distributions are calculated using a bin size of 1°, and the area under the probability density distribution curve is

normalized to 1. The normalization is done by first calculating the probability of occurrences of each angle in the sampled configurations, and then multiplying each angle's probability value by the bin size, that is, 1°.

Inspired by past studies, we quantify peptide–water and intra- and interpeptide hydrogen bonds to correlate them to the LCST-like behavior.<sup>7,10,14,36</sup> Hydrogen bonds exist when the distance between the hydrogen bonding donor and acceptor is less than 0.35 nm and the angle between acceptor atom, donor atom and hydrogen is less than 30°.<sup>68</sup> Within the total intrapeptide hydrogen bonds, we also separately calculate the intrapeptide backbone hydrogen bonds observed between the backbone carbonyl oxygen and amide hydrogens. The  $\beta$ ,  $\alpha$ , or  $\pi$  turn structure is defined as an intrapeptide backbone hydrogen bond formed between residues  $i$  and  $i + n$ , where ( $n = 3, 4$ , and  $5$ ). The turn is referred to as a  $\beta$ ,  $\alpha$ , or  $\pi$ -turn when  $n$  is 3, 4, or 5, respectively.<sup>69</sup> We use the last 200 ns (20000 time frames) and 100 ns (10000 time frames) for conducting the data analysis for the simulation of one free ELP chain and three tethered ELP chains, respectively. We report the mean and standard deviation of these 20000 or 10000 configurations.

**C. Coarse-Grained (CG) Simulations.** The CG model for ELP used in this work is a slightly modified version of the ELP model presented in Condon et al.<sup>10</sup> As in the original model of Condon et al.<sup>10</sup> (Figure 2a), in this work each ELP chain is modeled as a generic

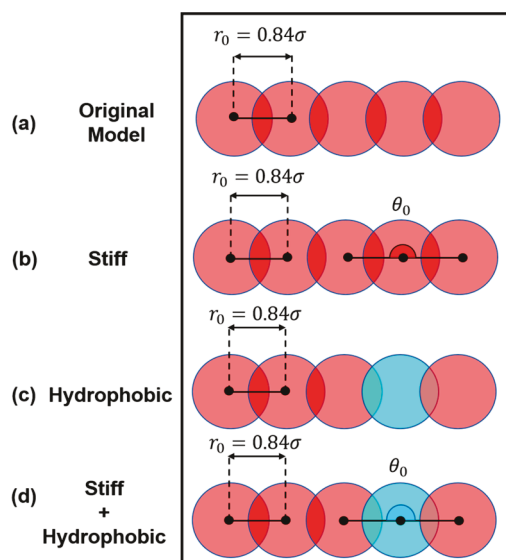


**Figure 2.** Schematic of the feature of the four ELP CG models used in this study. (a) Original CG ELP model of Condon et al.,<sup>10</sup> (b) new “stiff” ELP model that mimics the stiffness of the guest residue, (c) new “hydrophobic” ELP model that accounts for the hydrophobicity of the guest residue, and (d) hybrid “stiff and hydrophobic” ELP model that accounts for both the stiffness and the hydrophobicity of the guest residue.

bead–spring polymer, where each ELP bead (EB) represents a single amino acid. All ELP sequences contain 20 amino acids and, as a result, each CG ELP chain is modeled using 20 CG beads. The characteristic length,  $\sigma$ , and characteristic energy,  $\epsilon$ , for the ELP–CLP model are 0.5 nm and 0.1 kcal/mol, respectively. This choice of energy relates the reduced temperature  $T^* = 5.92$  to room temperature,  $T = 298$  K. The characteristic mass,  $m$ , is chosen arbitrarily as the goal of the ELP–CLP model is to capture the correct thermodynamics and not to capture the dynamics of these ELP–CLP systems. Therefore, the bead masses do not need to reproduce the exact masses of the residues they represent. So, each ELP bead has a mass of  $1.0m$  and a diameter of  $1.0\sigma$ . Adjacent bonded EB beads are connected via a harmonic bond potential, where the bond length is  $0.84\sigma$  and the force constant is  $1000\epsilon/\sigma^2$ . As in the original CG ELP model of Condon et al., we mimic the increasing tendency of an ELP chain to

collapse with increasing temperature using increasing attraction strength between nonbonded ELP CG beads,  $\epsilon_{EB}$ , within the Lennard-Jones (LJ) potential.<sup>70</sup>

$$U^{EB}(r) = \begin{cases} \epsilon_{EB} \left[ \left( \frac{\sigma_{EB}}{r} \right)^{12} - \left( \frac{\sigma_{EB}}{r} \right)^6 \right]; & r < 2.5\sigma_{EB} \\ 0 & ; \text{otherwise} \end{cases} \quad (3)$$

where  $\epsilon_{EB}$  is the interaction strength between nonbonded EB beads and  $\sigma_{EB}$  is the diameter of an ELP bead.

To test the hypothesis that the differences in local stiffness at/around the W and F guest residues impact the  $T_t$ , we have to modify the ELP model of Condon et al.<sup>10</sup> to include this stiffness through a harmonic angle potential on every fourth bead of each pentad in the ELP chain (Figure 2b). This harmonic bond angle is based on the bond angle distributions,  $P(\theta)$  versus  $\theta$ , obtained from atomistic simulations. First, Boltzmann inversion (BI) is used to obtain an initial guess of the potential of mean force (PMF) from atomistic bond angle distributions:  $U_{\text{angle}}^{\text{BI}}(\theta) = -k_B T \ln(P(\theta))$ , where  $k_B$  is the Boltzmann constant,  $T$  is the absolute temperature at which the atomistic simulation is performed, and  $P(\theta)$  is the corresponding atomistically obtained bond angle probability density distribution. Direct Boltzmann inversion is used instead of iterative Boltzmann inversion (IBI) as it is not possible to perform IBI using our CG ELP model that is not structurally mapped to the atomistic model. If one had to perform IBI, the PMF would be updated, iteratively, using bond angle distributions obtained from CG simulations with CG beads that are mapped to an atomistic model. The ELP model of Condon et al.,<sup>10</sup> is a generic polymer model that undergoes LCST-like transition where the increasing hydrophobicity effects upon increasing temperature are captured using an increasing effective attraction strength rather than through explicit CG temperature increases. Therefore, an exact one-to-one mapping between the atomistic simulations and the CG simulations is not possible, and thus, IBI is not a possible choice. To maintain brevity, all the details of the parametrization of bond-angle potentials are mentioned in Supporting Information (see Figures S4–S6; Tables S1 and S2).

Next, to test our second hypothesis that the differences in hydrophobicity of W and F and higher propensity for W to form  $\beta$ -hairpin structure in polypeptides than F together cause the trends in  $T_t$ , we define a new set of effective interactions only between W guest residues in our CG simulations. This new “W–W” effective interaction is different from the other ELP CG (EB) bead nonbonded interactions and encompasses the effective interactions between W residues because of hydrophobic interactions and secondary structure formation. We emphasize that we do not reproduce secondary structures using our CG model, and instead we incorporate the increased propensity of W-containing ELPs to form compact secondary structures by increasing the attraction strength of the interaction between W beads. Figure 2c shows a schematic depicting the new “hydrophobic” ELP model. In this model, the W-containing ELPs have two bead types: (1) generic EB beads which represent any residue besides the guest residue as in the original Condon et al.<sup>10</sup> work, and (2) W beads placed in 4th, 9th, 14th, and 19th position for WWWW and 9th and 14th position for FWWF. These new “W” beads have the same size, mass, and bonded interactions as other EB beads but the nonbonded W–W pairwise interactions are different from EB–EB and EB–W pairwise interactions. We use the ELP “hydrophobicity” scale of Urry et al.,<sup>12</sup> to calculate the well-depth of the W–W LJ potential.<sup>70</sup>

$$U^{W-W}(r) = \begin{cases} \epsilon_{W-W} \left[ \left( \frac{\sigma^W}{r} \right)^{12} - \left( \frac{\sigma^W}{r} \right)^6 \right]; & r < 2.5\sigma^W \\ 0 & ; \text{otherwise} \end{cases} \quad (4)$$

where  $\sigma^W$  is set at  $1.0\sigma$  and  $\epsilon_{W-W}$  is the interaction strength of W–W interactions defined relative to the interaction strength of EB–EB interactions ( $\epsilon_{EB}$ ). We use the difference in heats of substitution of phenylalanine (F) and tryptophan (W), as defined by Urry et al.<sup>12</sup> to obtain an estimate for the increased energetic contribution of W–W interactions (i.e., local hydrophobicity) relative to EB–EB interactions.

$$\epsilon_{W-W} = \epsilon_{EB} + 6\epsilon \quad (5)$$

where the difference in heats of substitution of phenylalanine (F) and tryptophan (W) (i.e.,  $\delta\Delta H(W) - \delta\Delta H(F)$ ) is determined to be 0.6 kcal/mol and is equivalent to  $6\epsilon$  using the characteristic energy of our CG model. We use the difference between the heats of substitution of F and W to incorporate the increased strength of W–W interactions, relative to F–F (i.e., EB–EB) interactions, in our CG model. We note that these differences in the heats of substitution of F and W suggest that W is more hydrophobic than F, which contradicts some of the other hydrophobicity scales that ranks F above W in hydrophobicity.<sup>50–54</sup> We choose to use the hydrophobicity scale of Urry et al.<sup>12</sup> because of the similarity in context (i.e., ELP inverse transition as a function of guest residue hydrophobicity) between their work and ours. Cross-interactions between W and EB beads are represented using the LJ potential with the interaction strength of cross-interactions equal to the interaction strength of EB–EB interactions (i.e.,  $\epsilon_{EB-W} = \epsilon_{EB}$ ). We note that in this context, since F–F interactions are captured by the EB–EB interactions, the FFFF CG model is the same as the original CG model in Figure 2a.

Lastly, to test if the combined effect of increased local stiffness and increased propensity of secondary structure of the W guest residue explain the differences in  $T_t$  as observed in experiments, we use a model shown in Figure 2d. In this model, the atomistically informed harmonic angle potential described in the “stiff” model and the new “W” guest residue bead are included when simulating WWWW and FWWF. For FFFF, this model is the same as the “stiff” model of Figure 2b.

Figure 3 shows a simulation snapshot of free ELPs and ELPs conjugated to CLP triple helix, where the CLP is modeled in the same way as described by Condon and Jayaraman.<sup>49</sup> The  $(\text{POG})_8$  sequence

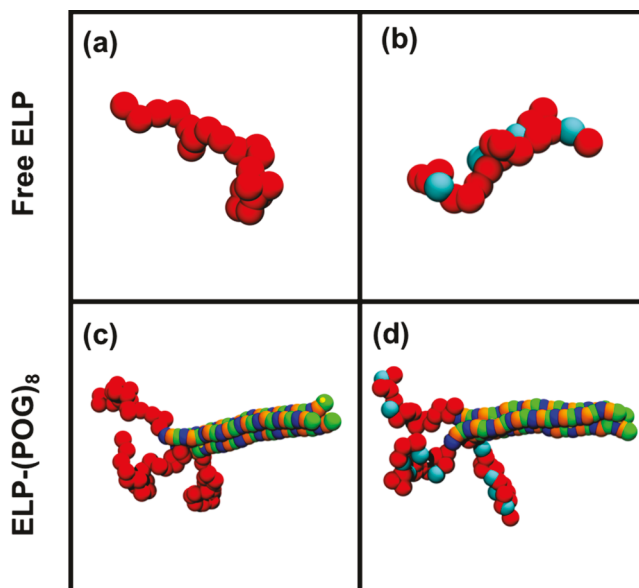


**Figure 3.** Schematic of CG models of free ELPs and ELP–CLP conjugates. (a) Free ELP (20-mer) with all EB beads (red), (b) free ELP (20-mer) with EB and “W” guest residue beads (cyan), (c) ELP–(POG)<sub>8</sub> conjugate, and (d) ELP–(POG)<sub>8</sub> conjugate with “W” residue beads. In the CLP triple helix (c, d) blue beads represent proline, orange beads represent hydroxyproline, and green beads represent glycine.

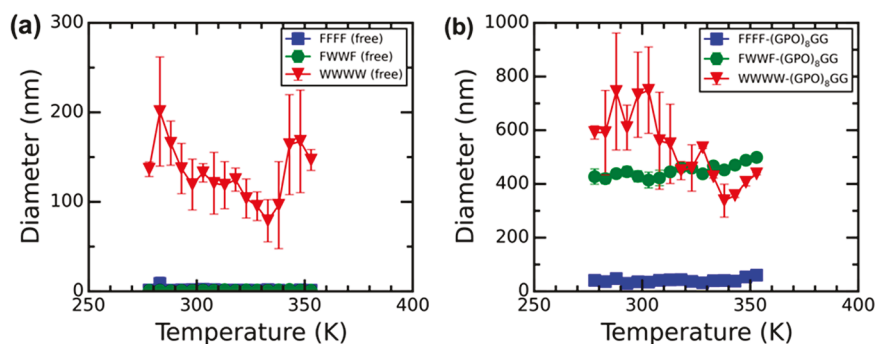


**Figure 4.** Average hydrodynamic diameter obtained from dynamic light scattering (DLS) characterization for (a) free ELPs and (b) ELP–CLPs. All samples are dissolved in DI water at a concentration of 1 mg/mL (no salt). ELP–CLP conjugates are incubated at 353 K for 10 min and cooled down at room temperature for overnight before measurement.

is used for CLP in all CG simulations to match the  $(\text{GPO})_8\text{GG}$  used in the experiments. The two sequences are equivalent, and the additional GG group, used in experiments to facilitate synthesis, is removed from our computational model as it does not affect the stability of the CLP triple helix. The GG group is added during experimental synthesis since it inhibits potential side reactions at the C-terminus of the CLP triple helix. The details of the CLP CG model have been reported in our original paper,<sup>49</sup> so only key features are presented here. Each CLP strand is a chain of POG triplets where each (POG) triplet is modeled using a proline backbone (PB) bead, a proline H-bond (PH) acceptor bead, a hydroxyproline backbone bead (OB), a glycine backbone (GB) bead, and a glycine H-bond (GH) donor bead. All backbone beads have a diameter of  $1.0\sigma$  and a mass of  $3.0m$ , while all H-bond beads have a diameter of  $0.3\sigma$  and a mass of  $1.0m$ . One of the impressive aspects of this model is that it captures the directionality and specificity of the inter-CLP strand H-bond interactions using a combination of bead sizes and isotropic, bonded and nonbonded, interactions involving the H-bond beads and the adjacent backbone beads. The details of the bonded and nonbonded interactions are described in the original paper.<sup>49</sup> It is important to note that the CG CLP model does not reproduce the experimentally observed helicity of the CLP triple helix but does capture the correct trends in how  $T_m$  of CLP triple helix varies with CLP design (i.e., length and composition), as described previously by Condon and Jayaraman.<sup>49</sup>

Using the above ELP and CLP coarse-grained models, we perform Langevin dynamics simulations in the NVT ensemble using the LAMMPS simulation package.<sup>71</sup> For free ELP simulations, the initial configuration is created by randomly placing 30 free ELP chains in a cubic simulation box of size  $140\sigma$  with periodic boundary conditions, achieving a concentration of approximately 0.1 mM. For ELP–CLP conjugates simulations, 10 ELP–CLP conjugates are randomly placed in a cubic simulation box with size  $140\sigma$  to maintain the same ELP concentration as the corresponding free ELP systems. The CLP triple helices are formed by placing three individual CLP single strands such that the backbone beads from each strand arrange in a triangular fashion, all along the CLP length, and all possible H-bonds between CLP strands are formed. Also, each strand is staggered from one another by one bead mimicking experimentally determined structures of CLP.<sup>49</sup> In all Langevin simulations, the friction coefficient is set to  $10\tau$  as done in Condon and Jayaraman.<sup>49</sup> We use a two-level RESPA<sup>72</sup> integrator so that nonbonded interactions are integrated with a time step of  $0.001\tau$  and bonded interactions are integrated with a time step of  $0.0005\tau$ . All systems are first equilibrated for  $10^8$  time steps followed by a  $10^7$  time step production run in which data is collected every 100000 time steps.

To distinguish the conformational states before and after the LCST-like transition of ELPs, we calculate the ensemble-average number of ELP bead pairwise contacts per ELP bead,  $\langle N_{\text{contacts per bead}} \rangle$ , as a function of ELP solvophobicity,  $\epsilon_{\text{EB}}$ . For simulations involving a single (EB) bead type, the number of ELP bead contacts only includes EB–EB contacts. For simulations involving the “W” and

EB beads, the total number of ELP bead contacts includes all possible combinations of ELP beads including EB–EB, EB–W, and W–W contacts and the total number of ELP beads is calculated as the sum of the number of EB and W beads. Next, for each frame in a simulation, the number of contacts is computed by counting the total number of unique ELP bead pairs which are separated by  $2.5\sigma$  or less, then dividing the total by the number of ELP beads in the simulation. Then the ensemble-average number of ELP bead contacts per ELP bead is calculated by averaging over all frames and the value is then averaged across three trials. The error bars shown in the results are the standard deviations across three trials. For all systems, the onset of aggregation is defined as the value of  $\epsilon_{\text{EB}}$  at which the plot of  $\langle N_{\text{contacts per bead}} \rangle$  versus  $\epsilon_{\text{EB}}$  reaches an inflection point.

### 3. RESULTS AND DISCUSSION

In Figure 4 we show the average hydrodynamic diameter obtained from dynamic light scattering (DLS) for each ELP and ELP–CLP conjugate. As illustrated in Figure 4a, free FFFF and FWWF ELPs exhibit hydrodynamic diameters less than 10 nm, indicating a lack of assembly between 278 and 353 K; the  $T_t$  of these two sequences are higher than 353 K. The WWWW ELP, in contrast, show evidence of assembly, with nanoparticle diameters of about 150 nm indicated at all measured temperatures (indicating that the  $T_t$  is lower than 278 K). These trends in  $T_t$  for these short ELPs are consistent with the experimental observations of Urry et al.<sup>12</sup> for long ELPs with  $>50$  kDa molecular weight. As illustrated in Figure 4b, the ELP–CLP conjugates WWWW-(GPO)<sub>8</sub>GG and FWWF-(GPO)<sub>8</sub>GG exhibit nanoparticles with hydrodynamic diameters of about 500 nm, indicating assembly, but no aggregates are observed for FFFF-(GPO)<sub>8</sub>GG throughout the range of temperatures (278–353 K) investigated. This trend indicates that the  $T_t$  values for WWWW-(GPO)<sub>8</sub>GG and FWWF-(GPO)<sub>8</sub>GG are less than 278 K, while the  $T_t$  of FFFF-(GPO)<sub>8</sub>GG is greater than 353 K. It should be noted that the  $T_t$  of FWWF in the conjugate decreases from 353 K (free FWWF) to less than 278 K (FWWF-(GPO)<sub>8</sub>GG), while for the other two peptides FFFF and WWWW, the shift in  $T_t$  before and after conjugation with CLP is not observed within the 278–353 K temperature range. The observed shift in  $T_t$  for FWWF upon conjugation with CLP is due to the local crowding of ELPs attached to CLPs, as explained in our previous work.<sup>10,38</sup> A summary of the observed trends in  $T_t$  from the DLS data is also mentioned in Table S3.

Based on the data presented in Figure 4, the WWWW-(GPO)<sub>8</sub>GG and FWWF-(GPO)<sub>8</sub>GG conjugates are expected to form ordered nanostructures in solution, similar to previous work of Luo and Kiick.<sup>38</sup> The detailed characterization of any

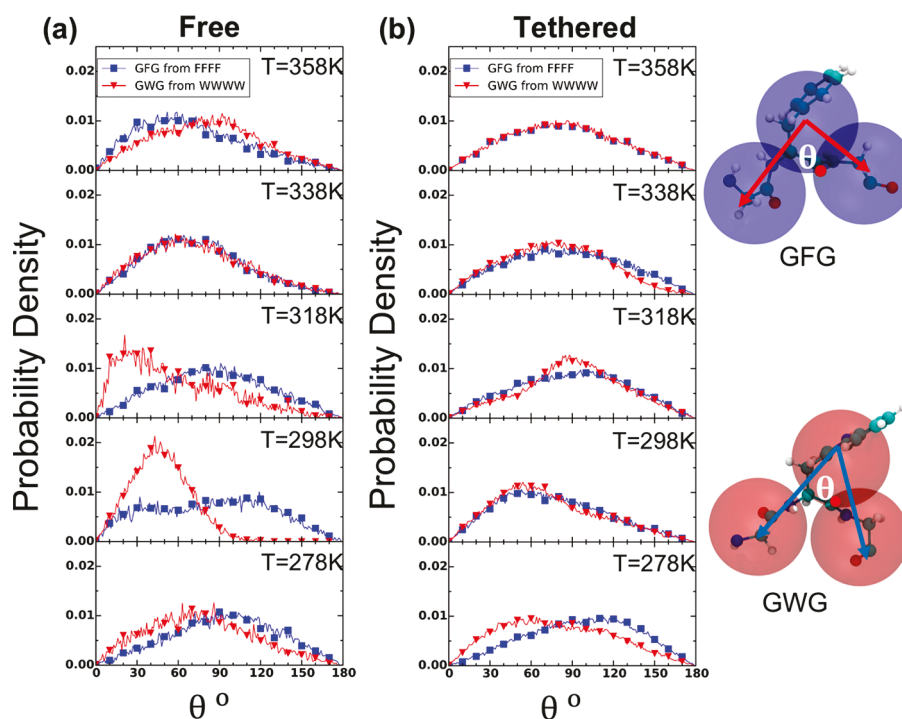


**Figure 5.** Local ( $G_{XX}G$ ) angle distribution in ELPs as a function of temperature from atomistic simulations. GFG is calculated from FFFF and GWG is calculated from WWWW in (a) free ELP and (b) tethered ELP systems.

nanostructures is outside the scope of this paper; here we focus on the molecular understanding of why and how the presence of guest residues W versus F impacts the  $T_t$  of ELPs and ELP–CLPs. A detailed description of the morphological features of the WWWW-(GPO)<sub>8</sub>GG and FWWF-(GPO)<sub>8</sub>GG nanostructures will be reported in due course.

To elucidate the molecular interactions that drive the above trends in  $T_t$  of ELPs and ELP–CLPs observed in Figure 4, we present the atomistic and CG molecular simulation results next.

First, we test our hypothesis that the  $T_t$  of WWWW is lower than that of FFFF due to the stiffness induced by the bulkier aromatic ring in W, which causes WWWW to have lower conformational entropy loss upon aggregation, leading to a lower  $T_t$  than FFFF. To estimate the stiffness of the ELP chain as a whole, we calculate the average persistence length of ELP  $C_{\alpha}$  atoms in the backbone chain in the atomistic simulations. The persistence lengths for all temperatures (278–370 K) in Figure S7 shows that the persistence length of FFFF and WWWW are effectively the same, within error. Next, we calculate the atomistically observed local bond angle distributions of  $G_{XX}G$  in VPG $X$ G. The GFG and GWG angle distributions from FFFF and WWWW systems are presented in Figure 5 and the corresponding data for FWWF are in Figure S8. In all cases, we observe that both GFG and GWG sample a wide range of angles. For free FFFF and free WWWW (Figure 5a), below 318 K, the GWG samples smaller angles than GFG, and above 338 K the GFG samples slightly smaller angles than GWG. The sampling of smaller angles can be understood as the acquisition of compact local structure and the local stiffness can be estimated from the probability density value of the average angle value. So, for free WWWW and FFFF, GWG adopts most stiff and compact structures at 298 and 318 K within the range of temperatures studied. For tethered FFFF and WWWW (Figure 5b), we observe that

GWG sample slightly smaller angles than GFG only at 278 K, while for all other temperatures the angle distributions of GFG and GWG are similar.

To explain if the above atomistically observed differences in local  $G_{XX}G$  angle distributions alone (i.e., local stiffness alone) can bring about the experimentally observed shifts in LCST-like behavior of ELPs and ELP–CLP conjugates, we use CG simulations. In Figure 6, all plots present the extent of ELP beads aggregation as a function of increasing attractive pairwise interactions among ELP beads ( $\epsilon_{EB}$ ); this increasing ELP bead aggregation with increasing  $\epsilon_{EB}$  serves as a mimic for the LCST-like transition of ELP chains with increasing temperature.<sup>10</sup>

In Figure 6a,b, we present results from CG simulations with the ELP CG model, which has atomistically informed angle potentials at the 4th, 9th, 14th, and 19th beads of any ELP chain and the same hydrophobicity through the ELP chain (as described in section 2C). We see that the inflection point (i.e., transition point) occurs at similar  $\epsilon_{EB}$  values for all free ELP cases (Figure 6a), indicating similar onset of aggregation irrespective of the local stiffness differences. A similar observation is made in ELP–CLP systems (Figure 6b). This suggests that the increased local stiffness of W in free ELPs is not the origin of the differences in the LCST-like transition, as shown in Figure 4 for FFFF, WWWW, and FWWF in free and CLP conjugated states. These CG simulations do show that the onset of aggregation of free ELP occurs at a higher  $\epsilon_{EB}$  than that of ELP–CLP systems (Figures 6a,b and S9). This is consistent with previous work<sup>10</sup> that showed that the increased crowding due to conjugation of ELP sequence (VPGFG)<sub>6</sub> to CLP led to a decrease in conformational entropy upon aggregation, thus, requiring a smaller energetic contribution to drive aggregation, in agreement with experimental observations of Luo and Kiick.<sup>38</sup> Our simulation results here in Figure 6 agree with our experimental results in Figure 4 of free FWWF

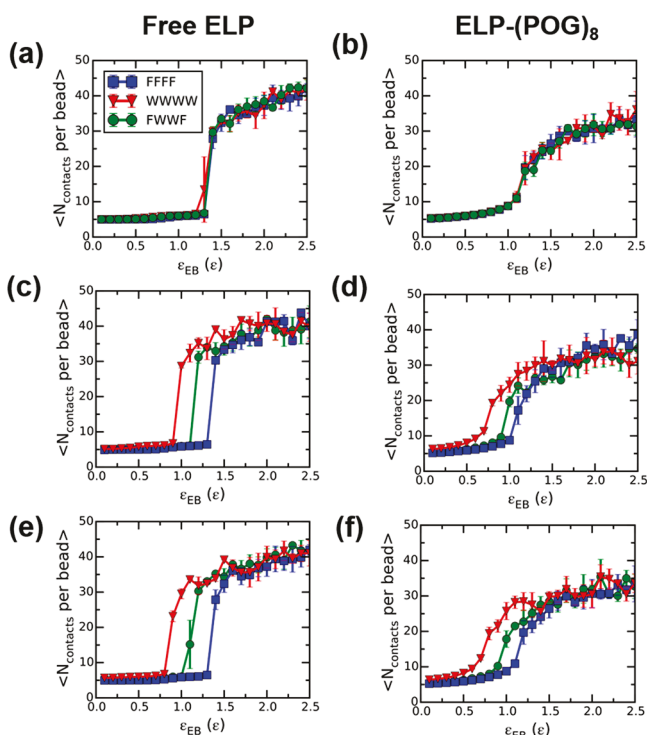


**Figure 6.** Ensemble average number of pairwise contacts per ELP CG bead vs the strength of attractive pairwise interactions among EB beads for (a, c, e) free ELPs and (b, d, f) ELPs conjugated with  $(\text{POG})_8$  CLP. Parts a and b are obtained using the “stiff” ELP model with atomistically informed CG angle potentials at the 4th, 9th, 14th, and 19th bead, but the same type of ELP bead throughout the ELP chain. Parts c and d are obtained using a “hydrophobic” ELP model with increased effective attraction for W in the ELP chains, but no angle potential throughout the ELP chain. Since FFFF does not have any W in it, this result for FFFF is essentially obtained with the same model as Condon et al.<sup>10</sup> FWWF has the increased hydrophobic W bead in the 9th and 14th place in the ELP chain and WWWW has the increased W bead in the 4th, 9th, 14th, and 19th place in the ELP chain. Parts e and f are obtained using “hydrophobic and stiff” ELP model with increased effective attraction for W (wherever it occurs) and atomistically informed CG angle potentials at the 4th, 9th, 14th, and 19th position in the ELP chains. Since FFFF does not have any W, this result for FFFF in parts e and f are the same as in parts a and b. FWWF and WWWW have the increased hydrophobicity at the 9th and 14th and 4th, 9th, 14th, and 19th positions, respectively.

and FWWF- $(\text{POG})_8$ , which also show an observable decrease in  $T_i$  for FWWF. While there is no experimental shift observed in FFFF and WWWW in Figure 4, we cannot say conclusively if there is an absence of a shift or if the shift in  $T_i$  is outside the experimental temperature range of 278–353 K.

To test our second hypothesis that the increasing propensity of secondary structure and hydrophobicity of W versus F cause the observed trends in  $T_i$ , we use the “hydrophobic” ELP CG model, which has no angle potentials, but an increased effective attraction of ELP CG “W” bead (as described in section 2C) at the 4th, 9th, 14th, and 19th positions of the WWWW ELP chains and at the 9th and 14th positions of the FWWF ELP chains. In Figure 6c, we see that with this updated model the free WWWW ELP has a lower transition point  $\epsilon_{\text{EB}}$  as compared to free FFFF and free FWWF. This shift toward a smaller energetic drive needed to aggregate ELP is consistent with the shift toward lower  $T_i$  in experiments. We see a similar shift in ELP-CLP systems shown in Figure 6d as well. The

difference between free ELP and ELP-CLP (e.g., free WWWW and WWWW-CLP) is similar to the difference between free ELP and ELP-CLP seen in the original Condon et al. work,<sup>10</sup> further confirming that the shift upon conjugation is driven by conformational entropy reasoning rather than by the higher propensity of W versus F to aggregate. Figure S9 shows the same data presented in Figure 6, but organized to facilitate a direct comparison of free ELP and ELP-CLP systems, showing the shift in the onset of aggregation of ELP upon conjugation to CLP.

So far, we have isolated the effects of local stiffness and the effects of increased hydrophobicity and increased propensity for secondary structure formation (combined into the increased effective W–W attraction). Figure 6e,f shows how the combination of the two factors above affects the onset of aggregation. Compared to Figure 6c, in Figure 6e, we observe an additional (by a small amount) reduction in the transition point  $\epsilon_{\text{EB}}$  for free WWWW, but not for free FWWF and free FFFF. For clarification, we direct the reader to Figure S10, which shows a direct comparison of the “hydrophobic” ELP model and “stiff and hydrophobic” model for FWWF and WWWW, in both free ELPs and ELP-CLP conjugates. This implies that the synergistic effect of stiffness, hydrophobicity, and propensity for formation of secondary structure can explain the shift for free ELPs, but only for the extreme case of WWWW.

While the above CG simulations elucidate the qualitative effect of stiffness, hydrophobicity and propensity for secondary structure on ELP aggregation in free and conjugated states at experimentally relevant concentrations, the coarse-grained implicit solvent representation of the ELP solution does not allow for explicit quantification of peptide–water and intra- and interpeptide hydrogen bonds and the secondary structures that may vary with W and F guest residues. Therefore, going back to the atomistic simulations we present this sort of structural information in Figures 7 and 8.

In Figure 7a the number of peptide–water hydrogen bonds as a function of temperature for FFFF, FWWF, and WWWW from one free ELP simulations shows that the peptide–water hydrogen bonds remained almost constant with temperature and is effectively the same for FFFF, FWWF, and WWWW. In Figure 7b we show a representative simulation snapshot that depicts peptide–water hydrogen bonds in one configuration of one free WWWW ELP chain. In Figure 7c, the intrapeptide hydrogen bonds versus temperature plot (depicted visually in Figure 7d) shows that the propensity to form intrapeptide hydrogen bonds is higher in WWWW at temperatures <338 K as compared to FFFF. This is in agreement with the experimental result in Figure 4a in which the free WWWW has larger aggregates than FFFF. In FWWF, while the intrapeptide hydrogen bonds are higher at 278 K as compared to FFFF, the FWWF and FFFF display a similar number of intrapeptide hydrogen bonds at remaining temperatures. This is also in agreement qualitatively with the observation that the FWWF and FFFF ELPs alone do not show significant differences in aggregation (Figure 4a). We note that when we say there is a higher propensity of WWWW to form intrapeptide hydrogen bonds as compared to FFFF, we also observe large fluctuations in intrapeptide hydrogen bonds. These results are from a one free ELP chain simulation, and the fluctuations suggest the ELP chain samples many configurations during the 400 ns simulations and is likely not kinetically trapped in one configuration.

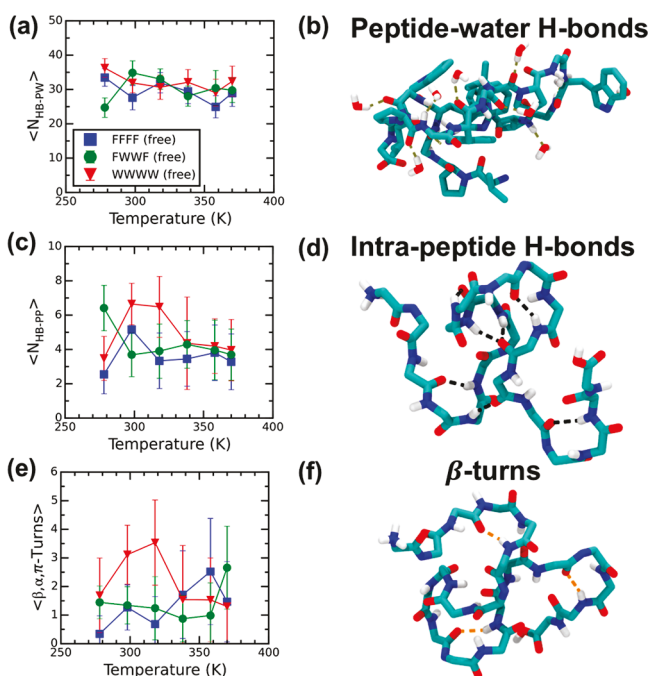


**Figure 7.** Number of hydrogen bonds between (a) peptide and water and (c) intrapeptide as a function of temperature. (e)  $\beta$ -,  $\alpha$ -, and  $\pi$ -turns in peptide as a function of temperature from one free ELP chain atomistic simulations. (b), (d), and (f) are simulation snapshots from one free WWWW system at 318 K representing the parameters plotted in the curves adjacent to the images. For clarity, the hydrogen atoms not contributing to H-bonds with water are not shown in part b; in parts d and f, the side chains are not shown and only hydrogen atoms attached to backbone nitrogen atoms are shown.

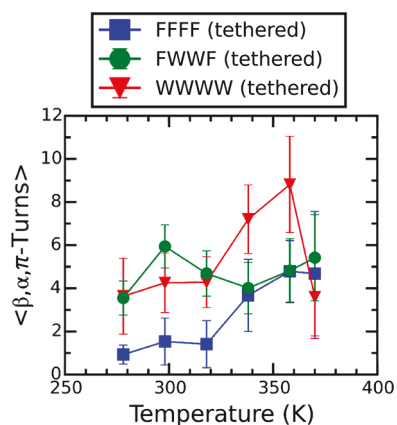


**Figure 8.**  $\beta$ -,  $\alpha$ -, and  $\pi$ -turns in peptide as a function of temperature from three tethered ELP chains atomistic simulation.

We also quantify the intrapeptide backbone hydrogen bonds stabilized secondary structure formation by calculating the number of  $\beta$ -,  $\alpha$ -, and  $\pi$ -turns. W is known to stabilize folded conformations of peptides through  $\beta$ -turns creating  $\beta$ -hairpins.<sup>56,57</sup> Figure 7e shows the average number of turn structure as a function of temperature in each system. WWWW has a higher propensity than FFFF to form these secondary structures at lower temperatures (<338 K). We also observe large fluctuations in turn structures similar to intrapeptide hydrogen bonds. To prove that the ELP chains are not kinetically trapped in one configuration in our system, we plot instantaneous values of  $\beta$ -,  $\alpha$ -, and  $\pi$ -turns for one particular

case in Figure S11, which clearly shows that the ELP chain samples many configurations. Further, our results are independent of the choice of time interval used for sampling as shown in Figure S12. Similar observations of transient  $\beta$ -turns are observed in highly dynamic and disordered ELP with three repeat units by Reichheld et al.<sup>34</sup> through NMR spectroscopy. They argued that the fluctuations in  $\beta$ -turns are due to the presence of water molecules near the peptide backbone which can also form hydrogen bonds with the peptide backbone. Above 338 K, the fluctuations in  $\beta$ -,  $\alpha$ -, and  $\pi$ -turn structure and intrapeptide hydrogen bonds increase, indicating that large vibrational motions of the peptide backbone can provide sufficient thermal excitation to break these hydrogen bonds. Rousseau et al.<sup>36</sup> have observed a similar trend in intrapeptide hydrogen bonds for GVG-(VPGVG) using MD simulations. Thus, the LCST-like behavior or structural transitions observed in free WWWW can indeed be related to the higher propensity of turn structure rather than simply a hydrophobic collapse of ELP.

We also compared the instantaneous fluctuations in end-to-end distance of backbone and values of  $\beta$ -,  $\alpha$ -, and  $\pi$ -turns for one free WWWW chain at 318 K, where we observed maximum number of  $\beta$ -,  $\alpha$ -, and  $\pi$ -turns, in Figure S11. These results do not clarify whether the ELP chain collapse occurs first or the turn structures are formed first.

We extend the above analysis of one free ELP (Figure 7) to three ELP chains tethered systems in Figure S13 and Figure 8. In Figure S13, we observe that the number of peptide-peptide hydrogen bonds for tethered FWWF is higher than tethered FFFF and tethered WWWW at temperatures <338 K while the number of water-peptide hydrogen bonds for tethered FWWF is smaller than tethered FFFF and tethered WWWW at temperatures <338 K. In Figure 8, the average number of  $\beta$ -,  $\alpha$ -, and  $\pi$ -turns for both tethered FWWF and WWWW are higher than tethered FFFF at temperatures less than 338 K. This suggests that in the tethered state FWWF will have a lower  $T_t$  than FFFF and similar or higher  $T_t$  for WWWW; this agrees with the experimental results in Figure 4. Furthermore, comparing Figure 7e and Figure 8, the key difference in the two is the upward shift in average number of turns for free FWWF (Figure 7e) to tethered FWWF (Figure 8), which is consistent with the experimental shift in Figure 4 going from FWWF to FWWF-(GPO)<sub>8</sub>GG conjugate. To prove that the tethered FWWF ELP chains are not kinetically trapped in one configuration near 298 K, where we observe an increase in the average number of  $\beta$ -,  $\alpha$ -, and  $\pi$ -turns in our system, we plot instantaneous values of  $\beta$ -,  $\alpha$ -, and  $\pi$ -turns in Figure S14, which clearly shows that the tethered FWWF chains sample many configurations. Thus, the experimental observation of aggregate formation for FWWF and WWWW, but not for FFFF, when they are conjugated to CLP, also correlates with a higher propensity for tethered FWWF and tethered WWWW to acquire secondary structure than FFFF.

#### 4. CONCLUSION

Through a combination of experiments, atomistic, and coarse-grained simulations, we show how and why the LCST-like transition temperature,  $T_t$ , of short elastin-like-peptides (ELPs), in free state and when conjugated to collagen-like peptides (CLPs), changes with the choice of guest residues (i.e., X in the VPGXG pentad). We choose the guest residue to be either F (phenylalanine) or W (tryptophan) which have the following differences: (i) the side chain of W has a bulkier

aromatic group likely causing higher local stiffness in W containing ELP chains than F containing ELP chains, (ii) W has been shown to form  $\beta$ -hairpins in polypeptides which could stabilize collapsed configurations at lower temperatures in W containing ELPs, and (iii) W and F are ranked higher and lower than each other in a variety of hydrophobicity scales. In our experiments, through dynamic light scattering (DLS) data we show that (VPGWG)<sub>4</sub> or WWWW has a lower  $T_t$  than (VPGFG)<sub>4</sub> or FFFF, in both free and conjugated to CLP states. Specifically, WWWW has a  $T_t < 278$  K while FFFF has a  $T_t > 353$  K in both free ELP and ELP–CLP systems. The  $T_t$  for FWWF ELP sequence decreases from being  $>353$  K for free ELP to  $<278$  K for ELP–CLP system. We know, based on our past work and consistent with simulation results here, that the decrease in  $T_t$  upon conjugation to CLP is due to crowding of ELP chains upon conjugation to CLP that decreases the conformational entropy loss upon ELP aggregation causing  $T_t$  to be lower in ELP–CLP compared to free ELP systems. To explain the trends in  $T_t$  with F/W guest residue substitution, we use a combination of atomistic and coarse-grained simulations. In our atomistic simulations, we find that free WWWW is more prone to adopt  $\beta$ -,  $\alpha$ -, and  $\pi$ -turns as compared to free FFFF and FWWF at lower temperatures ( $<338$  K). And, when conjugated with CLP, both FWWF and WWWW have a higher propensity to form  $\beta$ -,  $\alpha$ -, and  $\pi$ -turns at low temperatures. In simulations with atomistically informed CG models, we find that the increased local stiffness of W compared to F alone is not enough to explain the experimental shifts in  $T_t$  for WWWW versus FFFF. However, the combined effect of increased stiffness of W versus F and increased attractive W–W interactions compared to F–F interactions (based on hydrophobicity scales of Urry et al.<sup>12</sup> and increased propensity to acquire secondary structure) together show a shift in the onset of aggregation for free ELP and ELP–CLP systems consistent with the experimental shifts in  $T_t$ .

The results here demonstrate a way to fine-tune the  $T_t$  of ELPs and ELPs conjugated to CLP triple helix through the ELP pentad composition for short ELPs. This is useful for designing ELP and CLP containing materials that show stable nanostructures at temperatures in above the  $T_t$  of ELP and below the melting temperature,  $T_m$ , of the CLP triple helix. Being able to fine-tune the narrow range of temperatures between  $T_t$  and  $T_m$  where one can observe stable nanostructures creates many opportunities for designing biocompatible materials with ELP and CLP sequences. Additionally, this paper also demonstrates the value of combining atomistic and coarse-grained simulations to obtain a holistic view and complete understanding of biomacromolecules which often cannot be obtained by using just one of the above (atomistic or coarse-grained) approaches.

## ■ ASSOCIATED CONTENT

### 📄 Supporting Information

The Supporting Information is available free of charge on the ACS Publications website at DOI: [10.1021/acs.biomac.8b01503](https://doi.org/10.1021/acs.biomac.8b01503).

Data to obtain best fit bond angle potentials for coarse-grained simulations from atomistic simulations, bond angle distributions from atomistic simulations for GWG and GFG from FWWF; comparison of ensemble average number of ELP bead pairwise contacts for the hydrophobic ELP model and the stiff and hydrophobic

ELP model for free ELPs and ELP–(POG)<sub>8</sub> and number of hydrogen bonds between peptide and water; inter- and intrapeptide for tethered ELPs from atomistic simulations (PDF).

## ■ AUTHOR INFORMATION

### Corresponding Authors

\*E-mail: [kiick@udel.edu](mailto:kiick@udel.edu).

\*E-mail: [arthij@udel.edu](mailto:arthij@udel.edu).

### ORCID

Kristi L. Kiick: [0000-0001-8587-0301](https://orcid.org/0000-0001-8587-0301)

Arthi Jayaraman: [0000-0002-5295-4581](https://orcid.org/0000-0002-5295-4581)

### Author Contributions

†These authors contributed equally.

### Notes

The authors declare no competing financial interest.

## ■ ACKNOWLEDGMENTS

We thank the National Science Foundation (NSF) Grant 1703402 for financially supporting this work. Additionally, J.Q. and K.L.K. want to thank the National Institutes of Health (R21 AR069778A and 1 P30 GM110758) for partial financial support and instrument resources. The computational work in this paper was supported through the use of information technologies resources at the University of Delaware, specifically the Farber high-performance computing resources.

## ■ REFERENCES

- Urry, D. W. Free energy transduction in polypeptides and proteins based on inverse temperature transitions. *Prog. Biophys. Mol. Biol.* **1992**, *57* (1), 23–57.
- Vrhovski, B.; Weiss, A. S. Biochemistry of tropoelastin. *Eur. J. Biochem.* **1998**, *258* (1), 1–18.
- Gray, W. R.; Sandberg, L. B.; Foster, J. A. Molecular model for elastin structure and function. *Nature* **1973**, *246* (5434), 461.
- Urry, D. W.; Trapani, T.; Prasad, K. Phase-structure transitions of the elastin polypeptide model for elastin the framework of composition–temperature studies. *Biopolymers* **1985**, *24* (12), 2345–2356.
- Urry, D. W. Physical chemistry of biological free energy transduction as demonstrated by elastic protein-based polymers. *J. Phys. Chem. B* **1997**, *101* (51), 11007–11028.
- Martino, M.; Perri, T.; Tamburro, A. M. Biopolymers and biomaterials based on elastomeric proteins. *Macromol. Biosci.* **2002**, *2* (7), 319–328.
- Zhao, B.; Li, N. K.; Yingling, Y. G.; Hall, C. K. LCST behavior is manifested in a single molecule: elastin-like polypeptide (VPGVG) n. *Biomacromolecules* **2016**, *17* (1), 111–118.
- Meyer, D. E.; Chilkoti, A. Quantification of the effects of chain length and concentration on the thermal behavior of elastin-like polypeptides. *Biomacromolecules* **2004**, *5* (3), 846–851.
- Teeuwen, R. L.; de Wolf, F. A.; Zuilhof, H.; van Hest, J. C. Elastin-like polypeptides of different molecular weights show independent transition temperatures when mixed. *Soft Matter* **2009**, *5* (21), 4305–4310.
- Condon, J. E.; Martin, T. B.; Jayaraman, A. Effect of conjugation on phase transitions in thermoresponsive polymers: an atomistic and coarse-grained simulation study. *Soft Matter* **2017**, *13* (16), 2907–2918.
- Roberts, S.; Dzuricky, M.; Chilkoti, A. Elastin-like polypeptides as models of intrinsically disordered proteins. *FEBS Lett.* **2015**, *589* (19), 2477–2486.
- Urry, D. W.; Luan, C. H.; Parker, T. M.; Gowda, D. C.; Prasad, K. U.; Reid, M. C.; Safavy, A. Temperature of polypeptide inverse

temperature transition depends on mean residue hydrophobicity. *J. Am. Chem. Soc.* **1991**, *113* (11), 4346–4348.

(13) Reguera, J.; Urry, D. W.; Parker, T. M.; McPherson, D. T.; Rodríguez-Cabello, J. C. Effect of NaCl on the exothermic and endothermic components of the inverse temperature transition of a model elastin-like polymer. *Biomacromolecules* **2007**, *8* (2), 354–358.

(14) Li, N. K.; Roberts, S.; Quiroz, F. G.; Chilkoti, A.; Yingling, Y. G. Sequence directionality dramatically affects LCST behavior of elastin-like polypeptides. *Biomacromolecules* **2018**, *19* (7), 2496–2505.

(15) Girotti, A.; Reguera, J.; Arias, F. J.; Alonso, M.; Testera, A. M.; Rodríguez-Cabello, J. C. Influence of the molecular weight on the inverse temperature transition of a model genetically engineered elastin-like pH-responsive polymer. *Macromolecules* **2004**, *37* (9), 3396–3400.

(16) MacKay, J. A.; Callahan, D. J.; FitzGerald, K. N.; Chilkoti, A. Quantitative model of the phase behavior of recombinant pH-responsive elastin-like polypeptides. *Biomacromolecules* **2010**, *11* (11), 2873–2879.

(17) MacEwan, S. R.; Chilkoti, A. Digital switching of local arginine density in a genetically encoded self-assembled polypeptide nanoparticle controls cellular uptake. *Nano Lett.* **2012**, *12* (6), 3322–3328.

(18) Bidwell, G. L.; Raucher, D. Application of thermally responsive polypeptides directed against c-Myc transcriptional function for cancer therapy. *Mol. Cancer Ther.* **2005**, *4* (7), 1076–1085.

(19) Hyun, J.; Lee, W.-K.; Nath, N.; Chilkoti, A.; Zauscher, S. Capture and release of proteins on the nanoscale by stimuli-responsive elastin-like polypeptide “switches”. *J. Am. Chem. Soc.* **2004**, *126* (23), 7330–7335.

(20) Sallach, R. E.; Wei, M.; Biswas, N.; Conticello, V. P.; Lecommandoux, S.; Dluhy, R. A.; Chaikof, E. L. Micelle density regulated by a reversible switch of protein secondary structure. *J. Am. Chem. Soc.* **2006**, *128* (36), 12014–12019.

(21) Nettles, D. L.; Chilkoti, A.; Setton, L. A. Applications of elastin-like polypeptides in tissue engineering. *Adv. Drug Delivery Rev.* **2010**, *62* (15), 1479–1485.

(22) Betre, H.; Setton, L. A.; Meyer, D. E.; Chilkoti, A. Characterization of a genetically engineered elastin-like polypeptide for cartilaginous tissue repair. *Biomacromolecules* **2002**, *3* (5), 910–916.

(23) Zhang, Y. N.; Avery, R. K.; Vallmajo-Martin, Q.; Assmann, A.; Vegh, A.; Memic, A.; Olsen, B. D.; Annabi, N.; Khademhosseini, A. A highly elastic and rapidly crosslinkable elastin-like polypeptide-based hydrogel for biomedical applications. *Adv. Funct. Mater.* **2015**, *25* (30), 4814–4826.

(24) Ma, X.; Sun, C.; Huang, J.; Boutis, G. S. Thermal hysteresis in the backbone and side-chain dynamics of the elastin mimetic peptide [VPGVG]<sub>3</sub> revealed by 2H NMR. *J. Phys. Chem. B* **2012**, *116* (1), 555–564.

(25) Rodríguez-Cabello, J. C.; Alonso, M.; Pérez, T.; Herguedas, M. M. Differential scanning calorimetry study of the hydrophobic hydration of the elastin-based polypentapeptide, poly (VPGVG), from deficiency to excess of water. *Biopolymers* **2000**, *54* (4), 282–288.

(26) Li, B.; Alonso, D. O.; Daggett, V. The molecular basis for the inverse temperature transition of elastin I. *J. Mol. Biol.* **2001**, *305* (3), 581–592.

(27) Groß, P. C.; Possart, W.; Zeppezauer, M. An alternative structure model for the polypentapeptide in elastin. *Z. Naturforsch., C: J. Biosci.* **2003**, *58* (11–12), 873–878.

(28) Li, N. K.; Quiroz, F. G.; Hall, C. K.; Chilkoti, A.; Yingling, Y. G. Molecular description of the LCST behavior of an elastin-like polypeptide. *Biomacromolecules* **2014**, *15* (10), 3522–3530.

(29) Dandurand, J.; Samouillan, V.; Lacabanne, C.; Pepe, A.; Bochicchio, B. Water structure and elastin-like peptide aggregation. *J. Therm. Anal. Calorim.* **2015**, *120* (1), 419–426.

(30) Nuhn, H.; Klok, H.-A. Secondary structure formation and LCST behavior of short elastin-like peptides. *Biomacromolecules* **2008**, *9* (10), 2755–2763.

(31) Ahmed, Z.; Scaffidi, J. P.; Asher, S. A. Circular dichroism and UV-resonance Raman investigation of the temperature dependence of the conformations of linear and cyclic elastin. *Biopolymers* **2009**, *91* (1), 52–60.

(32) Cho, Y.; Sagle, L. B.; Iimura, S.; Zhang, Y.; Kherb, J.; Chilkoti, A.; Scholtz, J. M.; Cremer, P. S. Hydrogen bonding of of n. ke polype is stabilized in D2O. *J. Am. Chem. Soc.* **2009**, *131* (42), 15188–15193.

(33) Tang, J. D.; McAnany, C. E.; Mura, C.; Lampe, K. J. Toward a designable extracellular matrix: Molecular dynamics simulations of an engineered laminin-mimetic, elastin-like fusion protein. *Biomacromolecules* **2016**, *17* (10), 3222–3233.

(34) Reichheld, S. E.; Muiznieks, L. D.; Keeley, F. W.; Sharpe, S. Direct observation of structure and dynamics during phase separation of an elastomeric protein. *Proc. Natl. Acad. Sci. U. S. A.* **2017**, *114* (22), E4408–E4415.

(35) Krukau, A.; Brovchenko, I.; Geiger, A. Temperature-induced conformational transition of a model elastin-like peptide GVG (VPGVG) 3 in water. *Biomacromolecules* **2007**, *8* (7), 2196–2202.

(36) Rousseau, R.; Schreiner, E.; Kohlmeyer, A.; Marx, D. Temperature-dependent conformational transitions and hydrogen-bond dynamics of the elastin-like octapeptide GVG (VPGVG): a molecular-dynamics study. *Biophys. J.* **2004**, *86* (3), 1393–1407.

(37) Huang, J.; Sun, C.; Mitchell, O.; Ng, N.; Wang, Z. N.; Boutis, G. S. On the inverse temperature transition and development of an entropic elastomeric force of the elastin mimetic peptide [LGGVG] 3. *J. Chem. Phys.* **2012**, *136* (8), 08S101.

(38) Luo, T.; Kiick, K. L. Noncovalent modulation of the inverse temperature transition and self-assembly of elastin-b-collagen-like peptide bioconjugates. *J. Am. Chem. Soc.* **2015**, *137* (49), 15362–15365.

(39) Pechar, M.; Brus, J.; Kostka, L.; Koňák, Č.; Urbanová, M.; Šlouf, M. Thermoresponsive Self-Assembly of Short Elastin-Like Polypeptides and Their Poly (ethylene glycol) Derivatives. *Macromol. Biosci.* **2007**, *7* (1), 56–69.

(40) Nawroth, J. F.; McDaniel, J. R.; Chilkoti, A.; Jordan, R.; Luxenhofer, R. Maleimide-functionalized poly (2-Oxazoline)s and their conjugation to elastin-like polypeptides. *Macromol. Biosci.* **2016**, *16* (3), 322–333.

(41) Choi, H.; Chu, H.-S.; Chung, M.; Kim, B.; Won, J.-I. Synthesis and characterization of an ELP-conjugated liposome with thermosensitivity for controlled release of a drug. *Biotechnol. Bioprocess Eng.* **2016**, *21* (5), 620–626.

(42) Araújo, A.; Olsen, B. D.; Machado, A. V. Engineering Elastin-Like Polypeptide-Poly (ethylene glycol) Multiblock Physical Networks. *Biomacromolecules* **2018**, *19* (2), 329–339.

(43) Li, L.; Li, N. K.; Tu, Q.; Im, O.; Mo, C.-K.; Han, W.; Fuss, W. H.; Carroll, N. J.; Chilkoti, A.; Yingling, Y. G. Functional Modification of Silica through Enhanced Adsorption of Elastin-Like Polypeptide Block Copolymers. *Biomacromolecules* **2018**, *19* (2), 298–306.

(44) Luo, T.; Kiick, K. L. Collagen-like peptide bioconjugates. *Bioconjugate Chem.* **2017**, *28* (3), 816–827.

(45) Sakakibara, S.; Inouye, K.; Shudo, K.; Kishida, Y.; Kobayashi, Y.; Prockop, D. J. Synthesis of (Pro-Hyp-Gly) *n* of defined molecular weights Evidence for the stabilization of collagen triple helix by hydroxyproline. *Biochim. Biophys. Acta, Protein Struct.* **1973**, *303* (1), 198–202.

(46) Brodsky, B.; Ramshaw, J. A. The collagen triple-helix structure. *Matrix Biol.* **1997**, *15* (8–9), 545–554.

(47) Bella, J. Collagen structure: new tricks from a very old dog. *Biochem. J.* **2016**, *473* (8), 1001–1025.

(48) Brown, F., III; Hopfinger, A.; Blout, E. The collagen-like triple helix to random-chain transition: Experiment and theory. *J. Mol. Biol.* **1972**, *63* (1), 101–115.

(49) Condon, J. E.; Jayaraman, A. Development of a coarse-grained model of collagen-like peptide (CLP) for studies of CLP triple helix melting. *J. Phys. Chem. B* **2018**, *122* (6), 1929–1939.

(50) Hopp, T. P.; Woods, K. R. Prediction of protein antigenic determinants from amino acid sequences. *Proc. Natl. Acad. Sci. U. S. A.* **1981**, *78* (6), 3824–3828.

- (51) Kyte, J.; Doolittle, R. F. A simple method for displaying the hydrophobic character of a protein. *J. Mol. Biol.* **1982**, *157* (1), 105–132.
- (52) Von Heijne, G. Membrane protein structure prediction. *J. Mol. Biol.* **1992**, *225* (2), 487–494.
- (53) Monera, O. D.; Sereda, T. J.; Zhou, N. E.; Kay, C. M.; Hodges, R. S. Relationship of sidechain hydrophobicity and  $\alpha$ -helical propensity on the stability of the single-stranded amphipathic helix. *J. Pept. Sci.* **1995**, *1* (5), 319–329.
- (54) Boyd, D.; Schierle, C.; Beckwith, J. How many membrane proteins are there? *Protein Sci.* **1998**, *7* (1), 201–205.
- (55) Sheng, Y.-J.; Panagiotopoulos, A.; Kumar, S. Effect of chain stiffness on polymer phase behavior. *Macromolecules* **1996**, *29* (12), 4444–4446.
- (56) Cochran, A. G.; Tong, R. T.; Starovasnik, M. A.; Park, E. J.; McDowell, R. S.; Theaker, J.; Skelton, N. J. A minimal peptide scaffold for  $\beta$ -turn display: optimizing a strand position in disulfide-cyclized  $\beta$ -hairpins. *J. Am. Chem. Soc.* **2001**, *123* (4), 625–632.
- (57) Makwana, K. M.; Mahalakshmi, R. NMR analysis of tuning cross-strand Phe/Tyr/Trp-Trp interactions in designed  $\beta$ -hairpin peptides: Terminal switch from L to D amino acid as a strategy for  $\beta$ -hairpin capping. *J. Phys. Chem. B* **2015**, *119* (17), 5376–5385.
- (58) Amblard, M.; Fehrentz, J.-A.; Martinez, J.; Subra, G. Methods and protocols of modern solid phase peptide synthesis. *Mol. Biotechnol.* **2006**, *33* (3), 239–254.
- (59) Hess, B.; Kutzner, C.; Van Der Spoel, D.; Lindahl, E. GROMACS 4: algorithms for highly efficient, load-balanced, and scalable molecular simulation. *J. Chem. Theory Comput.* **2008**, *4* (3), 435–447.
- (60) The PyMOL molecular graphics system; <https://www.pymol.org/>.
- (61) Kaminski, G. A.; Friesner, R. A.; Tirado-Rives, J.; Jorgensen, W. L. Evaluation and reparametrization of the OPLS-AA force field for proteins via comparison with accurate quantum chemical calculations on peptides. *J. Phys. Chem. B* **2001**, *105* (28), 6474–6487.
- (62) Jorgensen, W. L.; Chandrasekhar, J.; Madura, J. D.; Impey, R. W.; Klein, M. L. Comparison of simple potential functions for simulating liquid water. *J. Chem. Phys.* **1983**, *79* (2), 926–935.
- (63) Hess, B.; Bekker, H.; Berendsen, H. J.; Fraaije, J. G. LINCS: a linear constraint solver for molecular simulations. *J. Comput. Chem.* **1997**, *18* (12), 1463–1472.
- (64) Bussi, G.; Donadio, D.; Parrinello, M. Canonical sampling through velocity rescaling. *J. Chem. Phys.* **2007**, *126* (1), No. 014101.
- (65) Berendsen, H. J.; Postma, J. v.; van Gunsteren, W. F.; DiNola, A.; Haak, J. Molecular dynamics with coupling to an external bath. *J. Chem. Phys.* **1984**, *81* (8), 3684–3690.
- (66) Darden, T.; York, D.; Pedersen, L. Particle mesh Ewald: An  $N \log(N)$  method for Ewald sums in large systems. *J. Chem. Phys.* **1993**, *98* (12), 10089–10092.
- (67) Cifra, P. Differences and limits in estimates of persistence length for semi-flexible macromolecules. *Polymer* **2004**, *45* (17), 5995–6002.
- (68) Luzar, A.; Chandler, D. Effect of environment on hydrogen bond dynamics in liquid water. *Phys. Rev. Lett.* **1996**, *76* (6), 928.
- (69) Kabsch, W.; Sander, C. Dictionary of protein secondary structure: pattern recognition of hydrogen-bonded and geometrical features. *Biopolymers* **1983**, *22* (12), 2577–2637.
- (70) Jones, J. E. On the determination of molecular fields.—II. From the equation of state of a gas. *Proc. R. Soc. London, Ser. A* **1924**, *106* (738), 463–477.
- (71) Plimpton, S. Fast parallel algorithms for short-range molecular dynamics. *J. Comput. Phys.* **1995**, *117* (1), 1–19.
- (72) Tuckerman, M.; Berne, B. J.; Martyna, G. J. Reversible multiple time scale molecular dynamics. *J. Chem. Phys.* **1992**, *97* (3), 1990–2001.